Cohesive granular columns collapsing: Numerics questioning failure, cohesion, and friction

Lydie Staron, Laurent Duchemin, Pierre-Yves Lagrée

Cohesive granular columns collapsing: numerics questioning failure, cohesion, and friction

Lydie Staron,[1] Laurent Duchemin,[2] and Pierre-Yves Lagrée[3]
[1)] *Sorbonne Université, CNRS - UMR 7190, Institut d'Alembert, F-75005 Paris, France*
[2)] *ESPCI Paris, UMR 7636 - Physique et Mécanique des Milieux Hétérogenes, F-75005 Paris, France*
[3)] *Sorbonne Université, CNRS - UMR 7190, Institut d'Alembert, F-75005 Paris, France*

(*Electronic mail: lydie.staron@sorbonne-universite.fr)

(Dated: 4 July 2023)

Simulations of the failure of cohesive granular steps with varying intensity of the contact adhesive force are presented. The simulations are compared with experimental and numerical study of wet shear flows[13,20], computing the apparent friction coefficient. We observe consistent behaviours. We reproduce the dependence between the macroscopic cohesion and the contact adhesion[2,11] observed experimentally for sticky polymer-coated grains, as well as the range of friction explored[15]. Focusing on the interface between moving and static material, and assuming a linear failure, we infer the orientation of the failure plane with the horizontal. We disclose a non-monotonous evolution with the intensity of the contact adhesion. Assuming an ideal Coulomb material allows for proposing an interpretation to this non-monotonous behaviour. Although the systems are past incipient failure, we consider an edge of material at equilibrium, for which the failure angle is related to the internal frictional properties of the material. In this framework, the non-monotonous evolution of the failure orientation may hint at a cohesion-induced weakening mechanism, by which stronger contact adhesion involve weaker friction.

I. INTRODUCTION

One enduring difficulty in describing the behaviour of granular media lies in their ability to adapt external forcing by changing behaviour, from flowing like a gas to resist shear like a solid[1]. Adding adhesion between the grains further obscures the picture: clogging in flows and size-dependent stability threshold mix up with effective viscosity and material properties in a way still to be clarified. Because cohesive granular materials are causing many problems in manufacturing techniques, significant work has been carried out in the engineering community to describe the various behaviour of cohesive material and characterise their properties[2–10]. Powders are mostly involved, namely very fine grains for which strong contact adhesion stems essentially from van der Waals forces. More academic considerations have also prompted numerous works[11–14]. The requirement for measurable well-constrained quantities often means using larger grains sticking together through capillary forces, which implies that weaker adhesive forces are accessible. Recently, the trade-off between cohesion control and cohesion strength has been mitigated by the design of a sticky polymeric coating, thus opening the way to more quantitative measurements at both low and high contact adhesion, and covering a large interval of macroscopic cohesion[15].

In this context, discrete numerical simulations can be of great help. Adding adhesive forces in the simulation contact model actually lead to unexpected outcome. Remarkably, Mandal et al (2020)[16], applying a smooth Discrete Element Method (DEM) approach, uncovered the role of the contact stiffness and restitution in the cohesive behaviour of the granular matter. Thereby they stress the need for the definition of an effective cohesion, in which contact adhesion does not play the sole part[16]. In the same line, non-smooth Contact Dynamics (CD) simulations show that the effective cohesion of granular samples increases with the mean duration of the contacts, embedded in the computational time step which reflects the non-smooth nature of the contact phenomena[17,18].

Consistent simulations allow for probing systems behaviour over a large range of parameters. For instance, the effect of contact adhesion on the macroscopic cohesive properties of the material can be explored[11–13,19–23]. This allows for discussing the initial theoretical model of Rumpf (1970)[2], revisited in Richefeu et al (2006)[11], predicting a linear relation between the cohesive strength, the structure of the packing and the contact adhesive force.

Studying the structure of the packing is made easier by numerical approaches, giving access to the details of the packing arrangements, showing an increase of the density of contacts with adhesion strength, and a decrease of the solid fraction[12,19,20,23,24]. The latter coincides with a strong expansion of the material and the emergence of stabilised loose structures when contact adhesion becomes large compared to the system average pressure[24,25].

The apparent friction μ^* of the material can also be computed, showing consistently an increase of μ^* with the macroscopic cohesion[13,20,24,25]. The study of Iordanoff et al (2005)[26] differs nevertheless: a non monotonous behaviour, with a decrease following the increase was observed, for large values of the cohesion. On the experimental side, Gans et al (2020)[15], who estimated the Coulomb friction, did not observe any significant variation of the later with the contact adhesion.

Most works addressing the behaviour of cohesive granular matter adopt a stationary, uniform configuration as annular or planar shear flow, simplifying the computation of mean averaged quantities over well-defined flow regimes. The configuration adopted in this study contrast with these conditions, since we are interested here in the failure of cohesive columns, which implies neither a uniform nor a stationary flow.

Beside, while most works on granular columns, including the

collapse of cohesive material, concentrate on the run-out behaviour or the deposit shape after the collapse[27–32], the present work focuses on the first instant of the failure. Assuming the failure to be a straight line opens an interesting way to explore the internal friction properties of the system. Although the hypothesis of a straight failure is a crude assumption if considered in the light of geomaterial science[33], it is nevertheless consistent with laboratory observation of the failure of model cohesive granular material[34], as well as continuum simulations[23,34].

In the following, we first discuss the choice of a failure criteria allowing for proposing a chronology of the instability, and the identification of the signature of the failure plane. We then evaluate the effect of the strength of the contact adhesion on the failure orientation, observing a non-monotonous behaviour. Computing the stress state of the simulated columns, and considering the equilibrium of an ideal Coulomb material, allows for questioning the mean behaviour of the granular matter in terms of internal friction. More specifically, we discuss the likeliness of a cohesion-induced weakening mechanism.

The numerical cohesive failures are presented in section II; the Contact Dynamics method and set-up are introduced in section II A, while II B details the unfolding of a failure. The identification of a robust criteria for characterising the failure event is discussed in section III, and the effect of adhesion strength on failure properties is presented. The stress state of the columns is analysed in section IV, and a Coulomb equilibrium is considered in section V. The hypothesis of an ideal Coulomb material is discussed in section VI, together with the possibility of a weakening mechanism induced by cohesion. The results are summarised in section VII.

II. COHESIVE FAILURES

A. Details of the simulations

a. Simulation method A Contact Dynamics algorithm was applied to simulate simple two-dimensional (2D) cohesive systems[17,35,36]. The grains are circular beads with a diameter randomly chosen in the interval $[4.10^{-3}\text{m}; 6.10^{-3}\text{m}]$, and a mean diameter $d = 5.10^{-3}\text{m}$, to prevent crystalline ordering. Each contact is made cohesive through the introduction of a negative (*i.e.* tensile) force threshold $-F_c$ in the Signorini's contact graph, which specifies the acceptable values for the contact normal force N. Either the distance δ between the grains is strictly positive, corresponding to a gap, and the contact force N is zero. Either $\delta = 0$, implying a contact, and N can take any values such that $N \geq -F_c$ compatible with the equations of dynamics. In addition, an Amontons-Coulomb friction law is implemented, involving the contact coefficient of friction μ_c. The tangential force threshold is supplemented with the adhesive force threshold: sliding is permitted when the tangential force has reached $\mu_c(N + F_c)$. The microscopic coefficient of friction is not varied: $\mu_c = 0.2$. The grains also interact through inelastic collisions, with a coefficient of restitution set to zero. Their volumetric density is $\rho = 0.1\,\text{kg.m}^{-2}$.

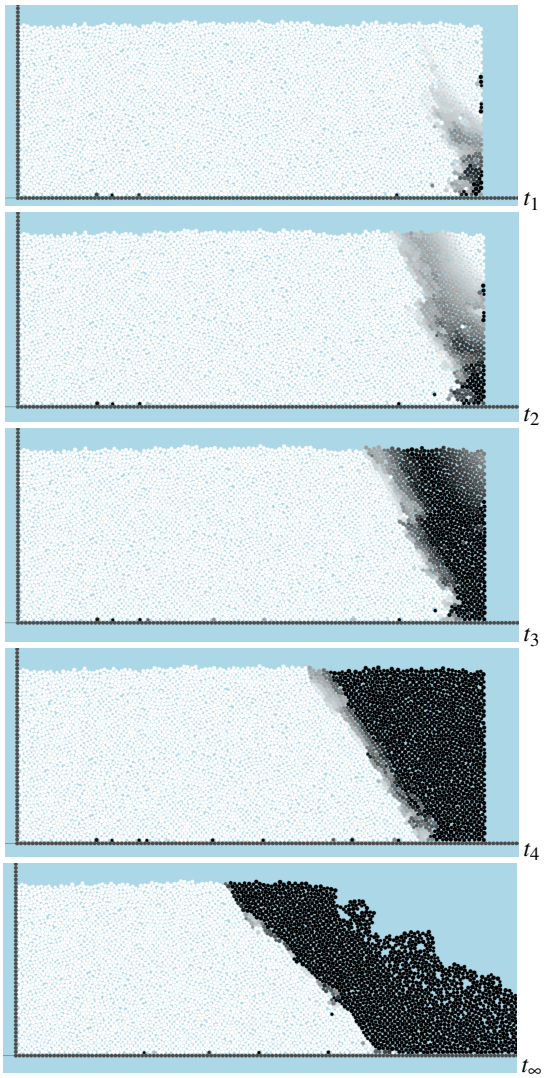

FIG. 1. Successive snapshots of the initiation of a failure in a cohesive granular step with a contact adhesion B_{og}= 30. The grey colour scale shows the grains cumulative displacement in the interval $]r_{th} : 1.4r_{th}]$, where $r_{th} = 0.1d$. Time shown are, from top to bottom, $t_1/T = 0.10$, $t_2/T = 0.11$, $t_3/T = 0.12$, $t_4/T = 0.17$ and $t_\infty/T = \infty$, $T = \sqrt{H/g} = 0.1515\,\text{s}$.

A comprehensive presentation of the CD method will be found in Radjai & Richefeu[17].

The adhesive force threshold F_c is given in number of grains mean weight through the introduction of a granular Bond number B_{og} [24,37]:

$$F_c = B_{og}\, m_{ij}\, g, \tag{1}$$

with $m_{ij} = 2(\frac{1}{m_i} + \frac{1}{m_j})^{-1}$, and i and j are the two grains in contact. Hence, the cohesive properties of the simulated systems will be set by the choice of the Bond number $B_{og}= F_c/mg$, giving the maximum adhesive resistance of contacts comparing to grain weight, which seems a sensible option since the failure sole driving is gravity. It is however a mere description of the contact adhesion, and not a

measurement nor an estimation of the macroscopic cohesive properties of the systems, which will be discussed in section VI.

Unlike numerical works modelling wet cohesive granular flows and describing cohesion as the result of capillary bonds[11,13,20,25], we do not assume a specific mechanism to induce contact adhesion. In particular, we do not assume a debonding or rupture distance for a cohesive contact to be lost. On the contrary, we assume adhesive force to be short-ranged, so that a cohesive contact is lost as soon as it opens. We simply make them sticky by allowing contact forces to exist in a tensile state. In that sense, our numerical systems are closer to the "controlled-cohesion granular material" of Gans et al (2020)[15] than to the "wet granular material" of Richefeu et al (2006)[11].

b. Generation of initial states The systems are generated by deposition under gravity of 5572 circular grains in a rectangular container. The grains are initially cohesionless with a weak contact friction $\mu_c = 0.2$, thus forming a dense packing with a volume fraction of $\phi \simeq 0.82$. When the systems have reached equilibrium, and all the grains are at rest, a large adhesive contact forces is applied in order to sinter the structure (B_{og}= 100, corresponding to a yielding height of roughly $50d$).

When launching the collapse simulation, the right wall closing the container is removed, and the Bond number is set to the desired value ($B_{og} \in [0,60]$). The systems thus reach the specified state of cohesion by decreasing the adhesion at initially sintered contacts, rather than increasing the adhesion at initially cohesionless contacts. In this way, we are ensuring that the failure is not induced by weaknesses in a contact network initially incompatible with cohesion.

The diameter of the grains is randomly chosen in the interval $[4.10^{-3}\text{m}; 6.10^{-3}\text{m}]$, with a mean diameter $d = 5.10^{-3}$m, to prevent crystalline ordering. The random function assigning the sequence of diameters allows for the generation of fundamentally different, independent initial states in terms of grains and contacts arrangement, yet with identical macroscopic dimensions. Following this procedure, 11 initial states were generated, and 11 independent runs could be performed for each value of the cohesion studied, totalling 132 independent runs, and allowing for the estimation of error bars.

The systems are bounded on the left hand side by a rigid vertical wall (Figure 1). The columns have an initial height $H \simeq 45d$ and a width $R \simeq 120d$, namely an aspect ratio $a \simeq 0.37$. This squat geometry allows for the generation of failures far enough from the left wall so that they remain unaffected by its presence.

B. Unfolding of a failure

At initial time $t = 0$, the right-hand-side wall is removed, and the columns are left to fail and spread onto a horizontal plane made rough by gluing grains on it (Figure 1). Because the present work is interested in the failure onset, and not on the ensuing spreading, we focus on the first instants of the evolution, recording the system state every $\Delta t = 10^{-3}$s. The computational time step is $dt = 2.10^{-4}$ s, coinciding with a mean grain overlap between $3.10^{-3}d$ (for B_{og}= 0) and $4.10^{-3}d$ (for B_{og}= 60).

The Bond number is successively set to B_{og}= 1, 2, 3, 4, 5, 10, 20, 30, 40, 50 and 60. In addition, the non-cohesive case B_{og}= 0 is also considered.

The column height $H \simeq 45d$ of the system, and the combination of contact adhesion explored, coincide with unstable states as studied in Abramian et al 2020 for similar systems[23]. If we suppose that the yielding height H_y satisfies $H_y/d \simeq 0.5B_{ond}$, as observed in[23], the systems studied here range from $H/H_y \simeq 1.5$ for B_{og}= 60, to $H/H_y \simeq 8$ for B_{og}= 10. For smaller B_{og} numbers, the predicted yielding height is smaller than $5d$. In that finite-size limit, the definition of a yielding height itself, according to a continuum picture of the systems, is no longer straightforward.

Figure 1 shows an example of the early instants of a failure, for B_{og}= 30. The present paper focuses on the analysis of system properties for a failure evolution corresponding roughly to the first four pictures. They coincide with a quasi-static part of the systems evolution, with a mean velocity of the order of $\sim 10^{-2}\sqrt{gH}$ (not shown).

The later stages of the evolution are nevertheless discussed in relation to the evolution of the stress tensor in section IV.

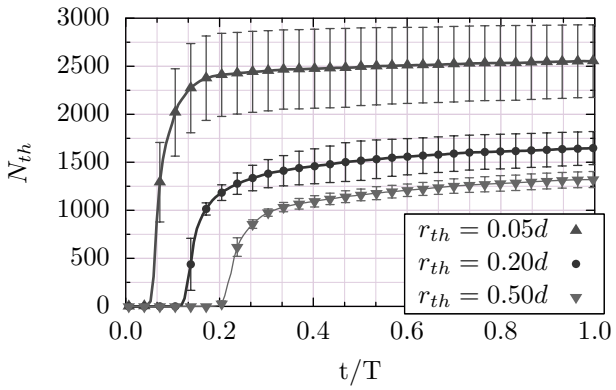

FIG. 2. Number of grains N_{th} whose cumulative displacement exceeds the displacement threshold r_{th} in the course of time, for three values of r_{th}, for a contact adhesion B_{og}= 30. The error bars show the corresponding standard deviation computed over 11 runs.

III. FAILURE CHARACTERISATION

In this section, we give the details of the method applied to detect the occurrence of the failure both in space and time. Because one aim of the study is to quantify the effect of cohesion onto the failure characteristics, the criteria must be valid and must carry the same information for any intensity of the contact adhesion. We explain here how this is achieved.

A. Defining a displacement threshold

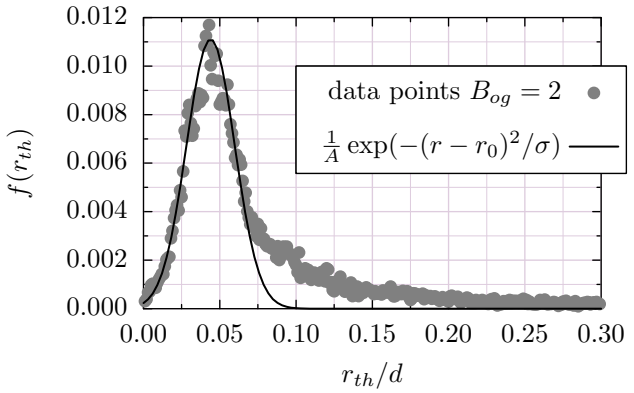

FIG. 3. Distribution of displacements over a time interval $[0,T]$, as a function of the displacement value r_{th}, and the gaussian approximation with $A = 90$, $r_0/d = 0.044$, and $\sigma = 0.1$; for B_{og}= 2.

A simple way of characterising the occurrence of a failure in a system of a few thousands grains is to track the displacement of the grains, without presuming the location of the displacement, nor its orientation. To this end, one needs to define a displacement threshold to separate those grains which have moved from those which will be considered static, considering that very small rearrangements in the bulk coexist with larger failure-induced motions[36].

For illustration, we show the behaviour of the simulation series with a contact adhesion B_{og}= 30 for three values of the displacement threshold $r_{\rm th}$. We consider $r_{\rm th} = 0.05d$, $r_{\rm th} = 0.20d$, and $r_{\rm th} = 0.50d$. We denote Δr_i the cumulative displacement of each grain i. For each value of $r_{\rm th}$, the number of grains $N_{\rm th}$ whose cumulative displacement Δr_i exceeds $r_{\rm th}$ is measured. The behaviour of $N_{\rm th}$ with time is displayed for B_{og}= 30 in Figure 2, averaged over 11 independent runs; the error bars show the corresponding standard deviation.

We observe, in each case, a sharp step-like evolution, with a distinct quick increase, which we identify as the onset of stability loss and the occurrence of a failure. A rapid saturation follows, which coincides with the flow of detached material running away with no significant number of additional grains further displaced beyond the value of the threshold.

Small values of $r_{\rm th}$ also probe diffuse motion of grains in the bulk, and induce large error bars. On the contrary, error bars nearly vanish for large displacement threshold. Yet focussing on large values of $r_{\rm th}$ also means that you miss out the early stages of the failure, with a risk of probing the erosion induced by the failure, rather than the failure itself.

To elect a value of $r_{\rm th}$ allowing for discriminating between diffusion-like motion and failure-induced motion, the distribution of displacements f over the time interval $[0,T]$ is considered. We compute the number of grains displaced in intervals $[r_{th}, r_{th}+0.001d]$, normalised by the total number of grains: $f(r_{th}) = \delta N_{th}/N_p = (N_{th}(r_{th}+10^{-3}d) - N_{th}(r_{th}))/N_p$, for r_{th} varying between $[0,5d]$. The outcome for a small value of contact adhesion B_{og}= 2 is plotted in Figure 3.

We observe that a gaussian behaviour is an acceptable approximation up to $r_{th}/d \simeq 0.07$, bespeaking a diffusion-like dynamics. Beyond $r_{th}/d \simeq 0.07$, the distribution deviates from a gaussian trend: additional small motions, presumably induced by the failure, contribute to the distribution. From $r_{th}/d \simeq 0.1$ onwards, the gaussian function vanishing suggests that small diffuse motion in this domain are caused by the failure dynamics only. In the following, to make sure that we do filter out all diffuse motion in the system, we chose twice this value to characterise the failure, namely $r_{\rm th}/d = 0.2$. Because more intense contact adhesion tends to shift the distribution towards smaller displacements, the threshold value $r_{\rm th}/d = 0.2$ is also adequate for larger values of the Bond number.

B. Identifying the failure chronology

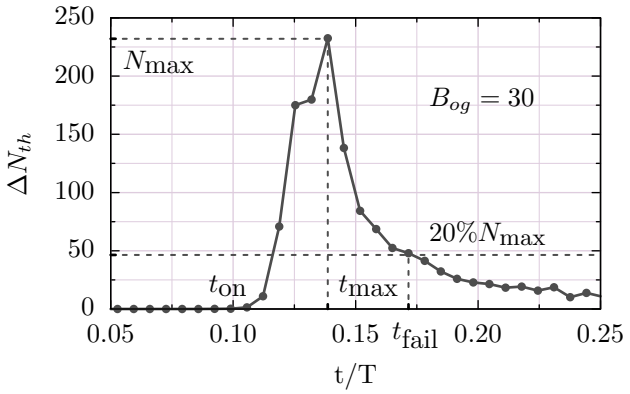

FIG. 4. Variations of the number of grains having overpassed the displacement threshold $r_{\rm th} = 0.20$d in the course of time, in the case of a contact adhesion B_{og}= 30. The onset time $t_{\rm on}$, the peak time $t_{\rm max}$, and the estimated failure time $t_{\rm fail}$, are also shown. ($T = \sqrt{H/g}$).

The smooth evolution of $N_{\rm th}$ with time allows for the identification of the onset of the stability loss, but not exactly the occurrence of a well-defined failure.

A natural choice is to detect an inflection point in the evolution of $N_{\rm th}$, simply plotting

$$\Delta N_{\rm th} = N_{\rm th}(t+\Delta t) - N_{\rm th}(t)$$

as a function of time, namely the instantaneous number of grains passing the displacement threshold $r_{\rm th}$ ($\Delta t = 1.10^{-3}$). For illustration, the first moments of the evolution of $\Delta N_{\rm th}$ for $r_{\rm th} = 0.20d$ and a contact adhesion B_{og}= 30 is plotted in Figure 4. A peak value – corresponding to the inflexion point– clearly comes out, after a rapid ascent bringing an increasing number of grains beyond the displacement threshold. A slower descent follows, corresponding to more localised motion involving fewer and fewer newly mobilised grains.

We define the time $t_{\rm on}$ at which motion onset is detected ($\Delta N_{\rm th} > 0$), and the time $t_{\rm max}$ at which the peak (maximum) value $N_{\rm max}$ is reached. Both $t_{\rm on}$ and $t_{\rm max}$ are specific for each

simulation. We find that they take well-defined values for each cohesion intensity. For instance, $t_{on}/T \simeq (0.111 \pm 8\%)$ and $t_{max}/T \simeq (0.140 \pm 5\%)$ for $B_{og} = 30$.

Singling out the best instant to characterise the failure occurrence is however difficult. The instant t_{max} of the peak value seems an obvious candidate. However, t_{max} coincides with an early state where a modest number of grains is mobilised. Moreover it does not offer a well-defined reproducible pattern for all values of the cohesion.

Hence we prefer to focus on a later stage of the evolution, when the failure has somewhat settled, and the number of newly mobilised grains has fallen from 80% of its maximum value. We denote the corresponding time t_{fail}. For the example case $B_{og} = 30$, we find $t_{fail}/T \simeq 0.157 \pm 5.7\%$. The graph in Figure 4 may give the feeling that t_{fail} is already at the end tail of the failure process; and certainly some grains mobilised at t_{fail} are responding to the beginning of the propagation of the failure rather than being a picture of its onset. However, plotting ΔN_{th} against the evolution of the mean grain velocity $\langle V \rangle / \sqrt{gd}$ shows that t_{fail} is still in the very first stage of the failure (not displayed). This can also be inferred from Figure 1, showing that the time interval in which t_{fail} falls (between t_3 and t_4), corresponds to imperceptible system deformations to the naked eye. Hence we do not expect the effect of failure propagation to be dominating.

C. Failure geometry

We now consider the position of the grains whose cumulative displacement Δr_i exceeds the threshold value $\Delta r_i \geq r_{th}$ at time t_{fail}. We then focus on the position of the grains at the interface between mobilised grains ($\Delta r_i \geq r_{th}$) and static grains ($\Delta r_i < r_{th}$), and consider that this interface forms a correct proxy of the shape of the failure.

An example is given in Figure 5 for the system displayed in Figure 1. We observe that the interface can be approximated by a straight line, the slope of which gives an estimation of the failure orientation α with the horizontal. The assumption of a linear failure is certainly in contradiction with observation of geomaterials behaviour[33,38]; yet it is consistent with experimental observation of cohesive granular failure. The cohesive granular material simulated in this work has no claim to resemble geomaterials. Straight lines being a quite convenient geometry to confront hypothesis, assuming linear failures seems a reasonable option.

The slope of the interface in Figure 5-b) is -1.90, with a regression standard error of 2.3%. Figure 5-c) shows the position of the grains displaced in the interval $[r_{th}, r_{th}(1+15\%)]$ at time t_{fail} for the same simulation, confirming that the interface between mobilised and static grains is a reliable signature of the failure geometry.

This analysis, discriminating between mobile and static grains applying a displacement binary criteria, resembles the outcome from image correlation technics. The latter, used in[34,39,40], reveal linear failure in collapsing cohesive columns. Continuum simulation of cohesive granular failures also reveal linear failure geometry in[32,34].

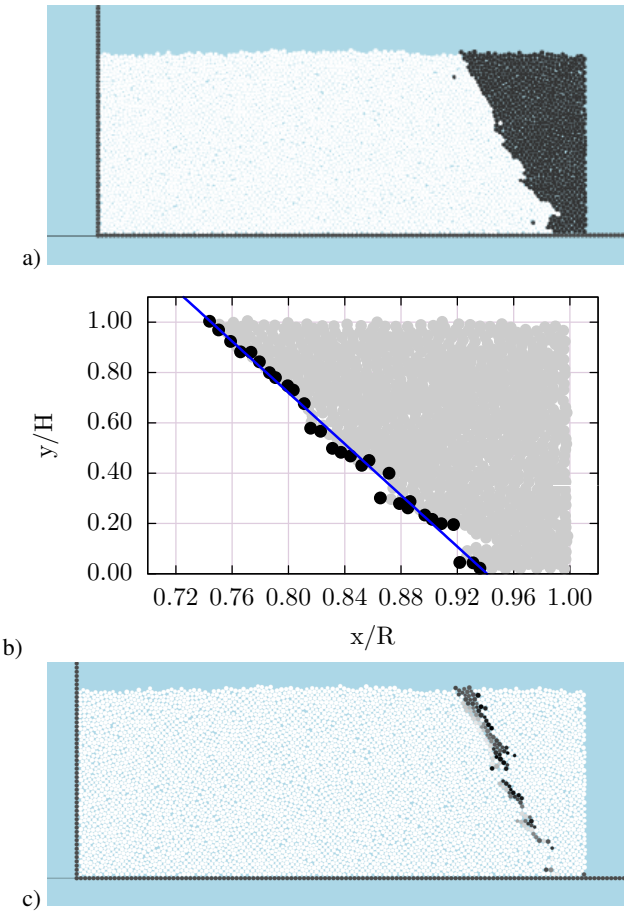

FIG. 5. **a)** Position of the grains whose cumulative displacement Δr_i exceeds the threshold value r_{th} at time t_{fail}: $\Delta r_i \geq r_{th}$ (in black), **b)** corresponding linear regression of the interface between static and mobilised region defining the failure orientation, **c)** position of the grains displaced in the interval $[r_{th}, r_{th}(1+15\%)]$ at time t_{fail} (grey shade).

D. Quality of the linear approximation

Contact adhesion changes the morphology of the failures. The shear band associated to small values of contact adhesion are wider, and less localised than those associated to larger contact adhesion. A a result, the linear approximation of the static/mobile interface shows larger standard error in the regression procedure for smaller contact adhesion (not to be mixed with the standard deviation measured from the set of values of α in each B_{og} simulation series). This can be seen in Figure 6, where the averaged asymptotic standard error (ASE) associated to the regression process in each simulation series is plotted against the value of the contact adhesion.

Figure 6 also shows the worst and best case scenario from all 132 simulations. The worst case scenario (from simulation series with $B_{og} = 3$) exhibits a linear approximation with a rather

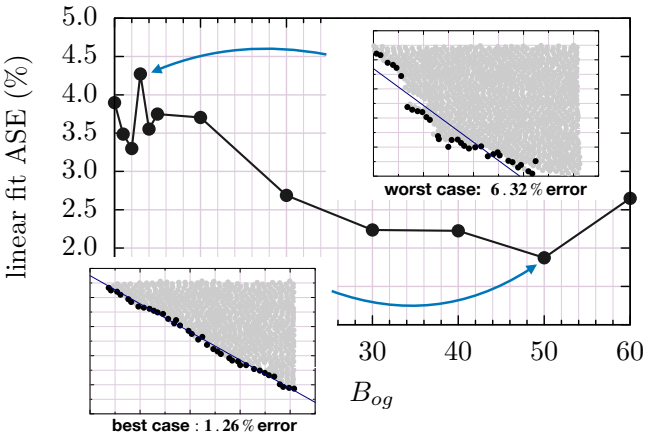

FIG. 6. Mean assymptotic standard error (ASE) of the linear approximation of the static/mobile interface as a function of contact adhesion B_{og}. The best case (error of 1.26% with $B_{og}=50$) and the worst case (error of 6.32% with $B_{og}=3$) taken from all 132 simulations, are shown for illustration.

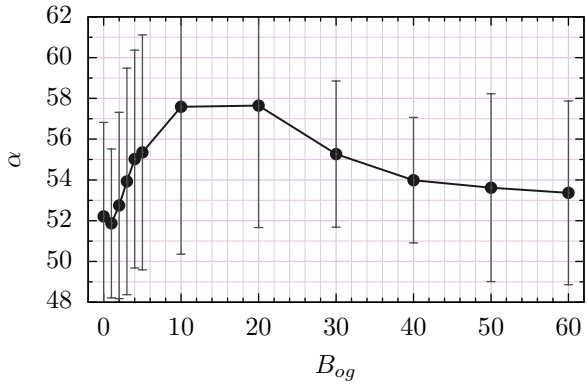

FIG. 7. Failure orientation with the horizontal α as a function of the contact adhesion Bond number B_{og}. The error bars show the corresponding standard deviation.

poor performance, yet not typical. Indeed, the associated error (6.32%) definitely overpasses the mean ASE for the set of simulations with $B_{og}=3$, which is 4.27%, and by far the mean ASE for all the weak adhesion interval $B_{og}\in[0:10]$, which is 3.71%. The best case scenario on the contrary exhibits a very neat line, which is more representative of the adhesion interval $B_{og}\in[20:60]$, if not strictly typical. Indeed, the associated error (1.26%) stands out less in this interval, which exhibits a mean ASE of 2.33%.

E. Cohesion and failure slope

Following the steps described above, we analyse all 11 independent simulations in each of the 12 simulations series in the adhesion interval $B_{og}\in[0:60]$. For each run, we estimate the orientation of the failure with the horizontal α. We also compute the corresponding standard deviation in each simulation series. The outcome is displayed in Figure 7. The first comment is that the error bars are large, showing the dispersion of the data. This is not a completely surprising fact for dry granular matter, for which static angles of repose, or avalanche size measured as the hysteresis angle, also exhibits a comparably large dispersion[41]. A second comment is that the amplitude of the contact adhesion seems to have no noticeable effect on the dispersion of the results, although it does affect positively the linear approximation of the failure (see subsection III D above).
The non-monotonous behaviour seems nevertheless a well-defined feature, with the slope of the failure increasing with contact adhesion for smaller values of the latter, but decreasing for stronger contact adhesion. In the following, we will discuss these results in terms of the frictional properties of the material, computing the apparent friction and considering a Mohr-Coulomb approach of cohesive granular media.

IV. COMPUTING THE APPARENT FRICTION

The failure and collapse of unconfined granular columns are strongly non-uniform and non-stationary events. This significantly affects the evolution of the stress state of the systems, as discussed in what follows.

A. The stress tensor

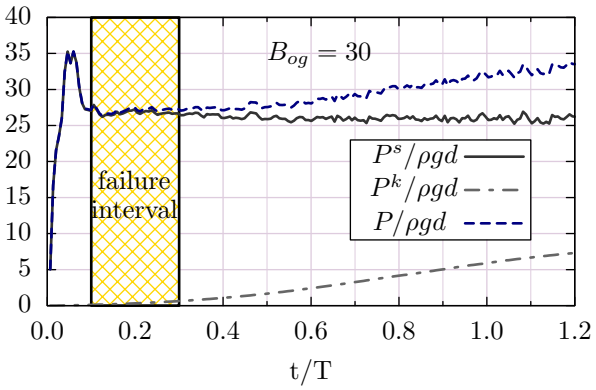

FIG. 8. Time evolution of pressure P^s, P^k and P computed from the static, kinetic and total stress tensors σ^s, σ^k and σ, here averaged on the simulation series with $B_{og}=30$. The shaded area shows the failure time interval (see text).

Stresses are computed following the classical micro-mechanical definition, including forces transmitted both by long-lasting contact interactions, and short-lived collisions induced by velocity fluctuations[20]. These two contributions, quantified by the static stress tensor σ^s and the kinetic stress

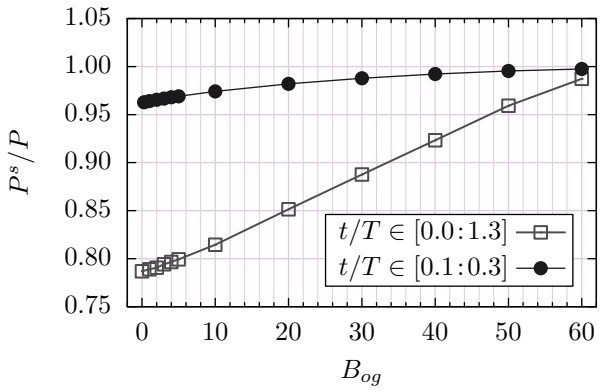

FIG. 9. Ratio of the pressure P^s measured by the static stress tensor σ^s to the total pressure P measured by the total stress tensor σ, evaluated over different time intervals. The static stress tensor is consistently dominating the total stress in the failure interval $t/T \in [0.1:0.3]$, during which the evolution is quasi-static or very slow ($P^s/P > 95\%$). We observe that strong adhesive forces favour the contribution of the static tensor, with the ratio P^s/P increasing with B_{og} in both time intervals.

tensor σ^k, form the total stress tensor σ:

$$\sigma = \sigma^s + \sigma^k,$$
$$\sigma = \frac{1}{V}\sum_{c\in N_c} \mathbf{f}^c \otimes \mathbf{r}^c + \frac{1}{V}\sum_{p\in N_p} m_p \delta\mathbf{v}^p \otimes \delta\mathbf{v}^p,$$

where $\mathbf{f}^c$ is the force transmitted by the contact c and $\mathbf{r}^c$ is the center-to-center vector, m_p is the mass, $\delta\mathbf{v}^p$ is the velocity fluctuation of grain p, N_c and N_p are the number of contacts and grains respectively over which the summation is made, V is the volume over which the stress is computed, and $\otimes$ is the dyadic product.

Figure 8 shows the pressure computed for each stress tensor σ^s, σ^k and σ, computed as the sum of the eigenvalues of each tensor, and denoted respectively P^s, P^k and P. The case B_{og}= 30 is chosen here for illustration. We observe a sudden jump of the static pressure P^s at the start of the simulation. This coincides with the sudden loss of cohesive contacts and the emergence of newly formed contact following the removal of the right-hand-side wall. We also see that the kinetic pressure P^k has a weaker contribution. It becomes however non negligible when $0.5 \lesssim t/T$, coinciding with the more dynamical part of the failure, when the pile starts collapsing. As a result, the total pressure P is dominated by the static stress in the first instants of the simulation, being equal or similar to P^s, but starts reflecting the kinetic stress as the material fails, at a later stage.

These features are shared by all simulations for any intensity of contact adhesion. However, the stronger the adhesion, the less significant the kinetic stress. Figure 9 shows the ratio of the static pressure P^s to the total pressure P as a function of B_{og}, averaged over two different time intervals. The first interval $t/T \in [0:1.3]$, or "collapse interval", spans the whole duration of the simulations, from the failure to the start of the spreading of the detached material. The second interval $t/T \in [0.1:0.3]$, or "failure interval" (shown in Figure 8), is focussing on the early instants of the failure, when the evolution is essentially quasi-static. We observe for both interval how adhesion favours the contribution of the static stress to the total stress state, with P^s/P increasing with B_{og}. More to the point, we see that the stress state is largely dominated by the static stress in the failure interval $t/T \in [0.1:0.3]$, where velocities, and thus kinetic stresses, are nearly zero. In the following, we will consider this failure interval $t/T \in [0.1:0.3]$ to evaluate the apparent friction associated to the failure onset.

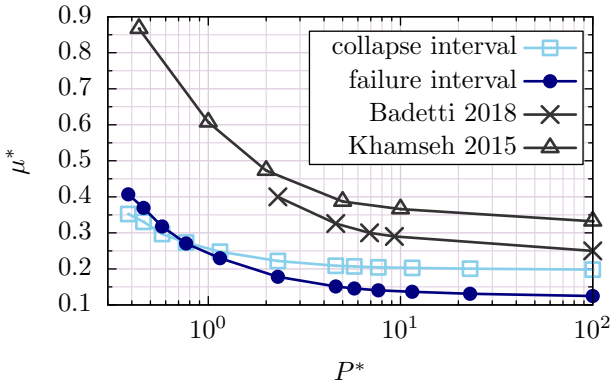

FIG. 10. Apparent friction μ^* computed in the failure time interval $t/T \in [0.1:0.3]$ and in the collapse time interval $t/T \in [0:1.3]$, as a function of the reduced pressure P^*. The data from[13,20] are also reproduced.

B. The apparent friction μ^*

The apparent friction μ^* is defined as the ratio of the deviatoric stress Q to the pressure P, both computed as functions of the eigenvalues of the total stress tensor σ: $\mu^* = Q/P$. Figure 10 shows the apparent friction μ^* measured and/or computed for sheared samples of wet granular matter as a function of the reduced pressure P^* in Khamseh et al 2015[20] and in Badetti et al 2018[13] (see**?** for details). The reduced pressure is defined as the ratio of the system characteristic pressure (or normal confining stress) and the characteristic adhesive stress, namely comparing the cohesion with the mean stress level of the system[13,20]. In the simulations discussed here, presenting unconfined failures, the only pressure stems from gravity. We thus define the reduced pressure P^* as the ratio of the gravity-induced pressure seen by the centre of mass of the packing $\frac{1}{2}\rho\phi gH$ (where ϕ is the solid fraction) divided by the contact adhesive stress F_c/d, thus giving $P^* = (2\phi H)/(\pi d B_{og}) \simeq 23/B_{og}$.

The simulations apparent friction μ^*, computed over the failure time interval $t/T \in [0.1:0.3]$, is displayed in Figure 10 together with the data from[13,20]. Note that we have artificially defined $P^* = 100$ for B_{og}= 0, in order to allow for comparison with the very low cohesion data from[13,20]. The behaviours are very comparable in terms of dependence on P^*, exhibiting a

marked increase with $1/P^*$. However, the values of μ^* of the simulations are much weaker, with $\mu^* \simeq 0.125$ for $P^* \to \infty$ and $\mu^* \simeq 0.4$ for $P^* \to 0$, instead of 0.33 and 0.87 observed by[20] for instance.

One may invoke a difference of contact friction, set to $\mu_c = 0.2$ in the present simulations. However, the data from[13,20], using respectively $\mu_c = 0.3$ and $\mu_c = 0.09$, both coincide with a larger apparent friction. Hence, the value of the contact friction does not provide any explanation.

Another source of discrepancy could be the flow regime in which the apparent friction is measured. While Khamseh 2015[20] and Badetti 2018[13] are considering flowing material under shear, the stress state of the simulations presented here is essentially measured over a static state. However, the flow inertial number I investigated in[13,20] spans a large interval including very small values: $I \in [10^{-4}, 5.10^{-1}]$, showing a continuity of behaviour, so that the gap between static and flowing regimes is bridged.
Interestingly though, in the present simulations, the apparent friction becomes larger when computed over the collapse interval $t/T \in [0 : 1.3]$, where the contribution of the kinetic stress becomes non-negligible (plotted on Figure 10). This is consistent with the observation of friction increasing with the inertial number for dry granular matter[42]. In our case, considering the collapse interval where the kinetic contribution is non-negligible, brings the apparent friction $P^* \to \infty$ from $\mu^* = 0.125$ to $\mu^\star \simeq 0.2$. This latter figure is consistent with the deposit slope of ~ 11.5 deg after the system has spread.

More relevant to friction might be the contact model chosen for simulating the granular media. Beside the differences between implicit CD and explicit DEM methods inherent to the algorithms,[13,20] are considering wet systems, where adhesive forces are capillary bridges. An essential feature of this type of adhesive interactions is the introduction of a debonding (or rupture) distance, at which the attractive force vanishes. The existence and extension of this debonding distance was shown to play a significant role in the value of the apparent friction[20]. By contrast, our cohesive samples are simple sticky beads, with short-ranged adhesion, for which attractive forces vanish as soon as contact is lost. In that sense, our systems resemble more the cohesion-controlled granular material designed by Gans et al (2020), for which no capillary bonds were observed[15]. Consistently, the present numerical observations are closer to the variations of friction with the contact adhesion observed experimentally by Gans et al, spanning a range of friction between 0.2 and 0.5 for a B_{og}varying between 5 and 50[?] .

V. A COULOMB EQUILIBRIUM MODEL

Assuming the cohesive granular systems to be an ideal Coulomb material gives us means of questioning the failure orientation α in terms of the material internal friction angle[43]. We consider a simplified equilibrium configuration along a linear failure following[23,34,44]. Although this geometry does not render the complexity of geotechnical observations, it reproduces experimental and numerical observation for model granular matter[34,36].

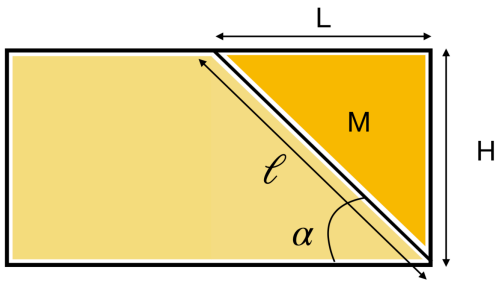

FIG. 11. Stability of a cohesive granular step: slip motion of a corner of mass M along the failure plane at incipient failure. L and H are respectively the horizontal extent of the failing corner and the height of the step; ℓ is the length of the failure plane, and α its orientation with the horizontal.

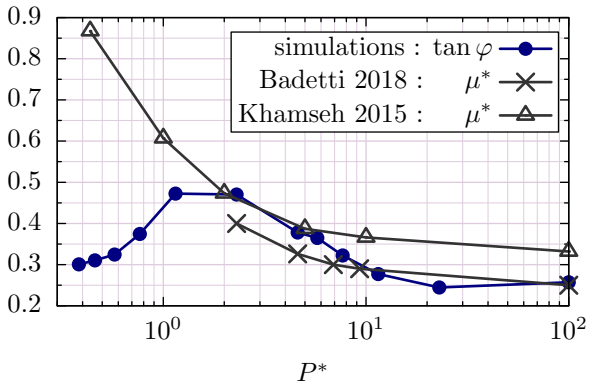

FIG. 12. Friction coefficient as a function of the reduced pressure P^* defined as: $\mu = \tan\varphi$ for the simulations, and as $\mu^* = \tau/\sigma_n$ for the experimental and numerical data from[13,20].

We suppose the equilibrium of the material along a failure plane of length ℓ, oriented at an angle α with the horizontal, as illustrated in Figure 11. Assuming that the shear stress τ and the normal stress σ_n satisfy the Mohr-Coulomb model, introducing a macroscopic cohesion τ_c, and a coefficient of internal friction μ, the equilibrium of the upper corner is compromised when

$$\tau = \mu\sigma_n + \tau_c,$$

leading to:

$$Mg\sin\alpha = \mu Mg\cos\alpha + \tau_c\ell, \tag{2}$$

where M is the mass of the failing part[23,34,44]. Denoting H the height of the step, and ρ the density of the material, we have $M = \frac{1}{2}\rho H^2/\tan\alpha$, and $\ell = H/\sin\alpha$. Equation (2) can readily be written in the form:

$$H = \frac{2\tau_c}{\rho g}\frac{1}{(\cos\alpha\sin\alpha - \mu\cos^2\alpha)} \tag{3}$$

which, considering the internal angle of friction φ such that $\mu = \tan\varphi$, becomes

$$H = \frac{2\tau_c}{\rho g}\frac{\cos\varphi}{\cos\alpha\sin(\alpha-\varphi)}. \quad (4)$$

The minimum height H_y of a failing step, namely a system just passed the equilibrium, is thus given by minimising the function $1/\cos\alpha\sin(\alpha-\varphi)$. The latter having a minimum at $\cos(2\alpha-\varphi)=0$, the failure orientation of a system of height H_y satisfies $\alpha = \pi/4+\varphi/2$. Conversely, the friction angle is given by $\varphi = 2(\alpha-\pi/4)$.
If the simulations were close to equilibrium, namely $H \simeq H_y$, the evolution of the failure orientation with cohesion in Figure 7 could be interpreted in terms of frictional properties. The coefficient of internal friction can be estimated as $\mu = \tan\varphi$, with equation (4) leading to $\varphi = 2(\alpha-\pi/4)$ at $H \simeq H_y$. The outcome for the numerical failures are plotted in Figure 12, together with the data from[13,20]. While $\varphi = 2(\alpha-\pi/4)$ increases with the strength of contact adhesion at small values of B_{og}, following the evolution of the failure orientation, a weakening mechanism would appear at larger B_{og} values, with friction slowly decreasing with increasing adhesion strength. Since stronger adhesive forces at contact between grains signify a more solid-like interface between two sliding blocks at failure, and less erratic dissipative collisions, stronger cohesion resulting in smaller friction seems a sensible scenario.

The decrease of friction properties with cohesion was (to our knowledge) only reported in a numerical study of the flow of the third body in Iordanoff et al 2005[26], considering plane shearing and intense values of contact adhesion. By contrast apparent friction increasing with cohesion is consistently observed experimentally and numerically[13,20,24].

However, applying $\varphi = 2(\alpha-\pi/4)$, which is a result stemming from a stability analysis when the yielding height H_y is just reached, is not a straightforward valid operation for our systems. Indeed, their height H is well above H_y for all values of B_{og} studied here (see section II B). Beside, α was shown to vary with the height of the systems[34,40,45]. Hence $\alpha(H > H_y)$ is not equivalent to $\alpha(H \simeq H_y)$ in terms of failure orientation, hence in terms of friction. Drawing definite conclusion on the frictional properties from the behaviour of α with B_{og} is thus not possible here.

VI. AN IDEAL COULOMB MATERIAL?

The equilibrium analysis performed above relies on the assumption that the cohesive granular material is an ideal Coulomb material, satisfying, at incipient slip, the simple relation between shear stress τ, normal stress σ_n, internal friction μ and cohesion τ_c[43]:

$$\tau = \mu\sigma_n + \tau_c.$$

The value of the macroscopic cohesion τ_c is not straightforward to estimate. For both experimental and numerical studies, τ_c is often derived from series of measurements of (τ,σ_n) for flows with a given cohesion; the locus of the affine approximation of the resulting set of points provides an estimate of τ_c[5,6,11,15]. Such a measurement is not feasible in the present collapse configuration.
We can however aim at an estimation of τ_c based on a theoretical prediction proposed in Richefeu et al 2006[11], and developed for 2D systems in Abramian et al 2020[23].
The analysis developed by Richefeu et al[11] from Rumpf equation[2] relates the value of the tensile strength, in the absence of confining pressure, to the contact adhesive interactions, and the structure of the packing, for a 3D wet granular media. We apply the same reasoning, modifying it for 2D quasi-mono-disperse systems, and using expression (1) for the contact adhesive force F_c, rather than capillary forces. Following[11], the density of cohesive contacts Z_c is given by half the mean number of cohesive contacts per particle, divided by the particle free volume in 2D (*i.e.* the average particle volume $V_p = \pi d^2/4$ divided by the solid fraction ϕ):

$$\sigma_c = \frac{\phi Z_c}{\pi d}F_c, \quad (5)$$

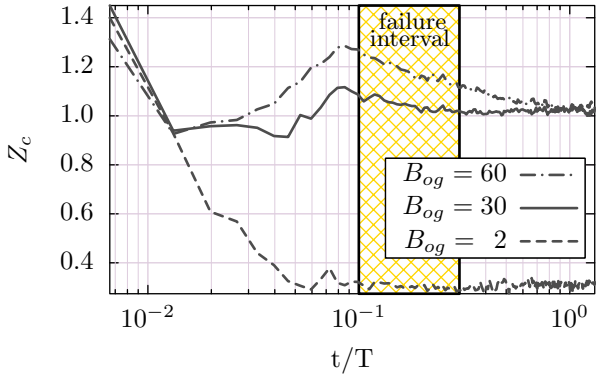

FIG. 13. Density of cohesive contacts Z_c as a function of time for three different values of contact adhesion B_{og}.

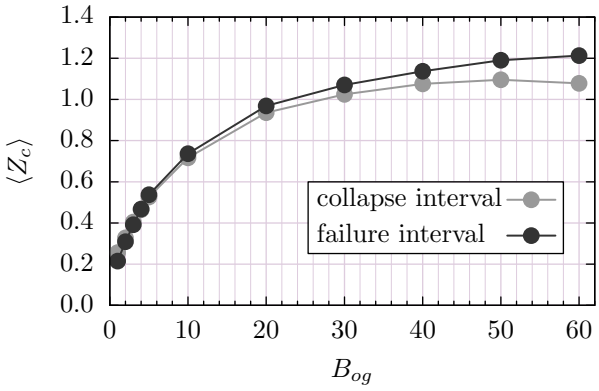

FIG. 14. Mean density of cohesive contacts $\langle Z_c \rangle$ as a function of the contact adhesion B_{og} number, computed over the collapse time interval $t/T \in [0:1.3]$ and the failure time interval $t/T \in [0.1:0.3]$.

with ϕ the packing volume fraction and Z_c the mean number of cohesive contacts per particle. Considering the contact adhesive forces $F_c = mgB_{og} = \rho g V_p B_{og}$, the theoretical prediction for the macroscopic cohesion of an assembly of cohesive particles $\tau_c = \mu\sigma_c$ is given by:

$$\tau_c = \frac{d}{4}\mu\phi Z_c \times \rho g \times B_{og}, \qquad (6)$$

where μ is the internal coefficient of friction.
Since the present simulations involve initial states prepared using a zero friction to generate dense packings, sintered afterwards using a large value of contact adhesion B_{og}= 100, all our systems present a large initial packing fraction $\phi \simeq 0.82$, which does not vary until the failure crack has developed. In the following, we will thus consider the constant value $\phi = 0.82$.
Estimating τ_c also requires that we have an estimate for the internal friction μ, different from the apparent friction μ^* computed in section IV. We simply set $\mu = 0.3$, which seems a reasonable value.
Finally, we need to estimate Z_c. Although any contact can withstand a tensile state, not all contact do exist in this peculiar state. In the following, we consider a contact to be cohesive if it actually carries a tensile force. The time evolution of Z_c for three values of B_{og}, corresponding to a weak, medium and strong contact adhesion, is shown in Figure 13. Plotting Z_c as a function of B_{og}, averaged over either the collapse interval or the failure interval, shows how larger contact adhesion coincides with a larger density of cohesive contacts (displayed in Figure 14): $Z_c \simeq 0.3$ for B_{og}= 2, while $Z_c \simeq 1.2$ for B_{og}= 60. For comparison, the mean number of contacts per particle (or "coordinance"), is around 3.5.

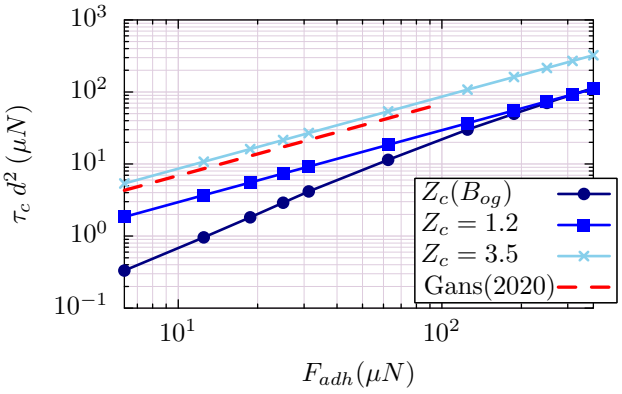

FIG. 15. Relation between the theoretical prediction of the macroscopic cohesive stress $\tau_c d^2$ (equation (6)) and the contact adhesive force F_{adh} for different value of the density of cohesive contacts Z_c. The dashed line shows the prediction for the experimental data from Gans 2020[15], together with the corresponding range of values.

In a first try, we estimate the cohesive stress τ_c considering the value of Z_c for each series of simulations independently, as they are given in Figure 14 for the failure interval. The outcome of relation (6) is plotted Figure 15. Expectedly, the plot reflects the behaviour of $Z_c(B_{og})$ in Figure 14.
In a second try, following[11,15], we take a constant value for Z_c. We set $Z_c = 1.2$, corresponding to the case B_{og}= 60. The plot becomes linear, but with a lower proportionality constant than the prediction describing the experimental data from[15], due to the fact that we have not considered that all contacts are cohesive as in[11,15].
Eventually, if we consider that all contacts are cohesive following[11,15], equating Z_c with the grains mean coordination number $Z_c = 3.5$, the result of the simulations becomes very similar to that of Gans et al (2020)[15].
Figure 15 is a good illustration of the way the relation between macroscopic stress and contact adhesion is very dependent on the details of the cohesive texture and the way it is estimated. It also shows that the numerical cohesive matter simulated here behaves very similarly to the experimental cohesion-controlled material of Gans et al[15] in terms of the dependance $\tau_c \propto F_c$.
However, Gans et al 2020[15], as we did, assume a constant coefficient μ. A constant volume fraction ϕ, and a constant density of cohesive contacts, are also chosen. The latter are however very dependant on the system cohesion[24,25]. Hence, Figure 15 and the linearity of the relation $\tau_c \propto F_c/d$ does not give informations on the dependence of τ_c on the internal friction.
If the material obeys an ideal Coulomb behaviour, the stress state satisfies $\tau = \mu\sigma_n + \tau_c$. It $\tau_c = \mu\sigma_c$, then $\mu = \tau/(\sigma_n - \sigma_c)$, and an increase of the contact adhesion and of σ_c may coincide with an increase of μ. If we do not assume $\tau_c = \mu\sigma_c$, we have $\mu = (\tau - \tau_c)/\sigma_n$, and an increase of the contact adhesion and of τ_c may coincide with a decrease of μ.

This is what is observed in Iordanoff et al (2005)[26], although the apparent friction (and not the Coulombic friction) is considered. Another difference is that [26] considers much smaller values of the reduced pressure P^* (about 10 times smaller), *i.e.* much stronger adhesive forces. Iordanoff et al (2005) attribute the decrease of friction with adhesion to the thinning of the shear zone where grains are irreversibly deformed. In that sense, their observation bears analogy with the scenario proposed in the present paper (section V), invoking a failure plane resembling more and more a solid-solid sliding interface when contact adhesion increases, and resembling less and less a collection of erratically colliding particles dissipating energy.

VII. DISCUSSION

Simulation of the failure of cohesive granular steps, with varying intensity of the contact adhesive force, are presented. Failures are characterised through a careful analysis of the grains displacement, which allows for deriving a chronology of the failure events. Focusing on the interface between moving and static material, we infer the position of the failure plane, found to be compatible with a linear shape, in agreement with previous observations[34,36,40]. Plotting the

failure orientation with the horizontal against the intensity of the contact adhesion, we disclose a non-monotonous evolution.

Although the column collapse is an intrinsically transient heterogenous phenomena, it can be compared with experimental and numerical study of wet shear flows[13,20], provided we adopt a definition of the reduced pressure relevant to the collapse configuration. Doing so, and computing the apparent friction coefficient, we observe consistent behaviours. The weak values of friction in our simulation points at the short-range of the contact adhesion model implemented here, which does not consider any debonding distance characteristic of capillary cohesion[20]. Our model nevertheless reproduces the behaviour of sticky polymer-coated grains[15], in particular the dependence between the macroscopic cohesion and the contact adhesion, and the range of friction explored.

Assuming that the material behaves as an ideal Coulomb material allows for writing the equilibrium of an edge of material at incipient failure, for which the failure angle is related to the internal frictional properties of the material. This provides an interpretation of the non-monotonous behaviour of the orientation of the failure plane. Although the systems studied here are past equilibrium and incipient failure, the non-monotonous evolution of the failure orientation may hint at a cohesion-induced weakening mechanism, by which stronger contact adhesion involves weaker friction.

ACKNOWLEDGMENTS

The authors acknowledge a very fruitful reviewing process.

[1]H. M. Jaeger, S. R. Nagel, R. P. Behringer, Granular solids, liquids, and gases, Rev. Mod. Phys. **68**, 1259 (1996).

[2]Rumpf, H.C.H., Zur Theorie der Zugfestigkeit von Agglomeraten bei Kraftübertragung an Kontaktpunkten. Chemie Ingenieur Technik, **42**: 538-540 (1970).

[3]H. Schubert, Capillary forces - modeling and application in particulate technology, Powder Technology **37**, 1, (105-116), (1984).

[4]Jenike, Andrew W.. "A theory of flow of particulate solids in converging and diverging channels based on a conical yield function." Powder Technology **50**: 229-236 (1987).

[5]P. Pierrat, D. K. Agrawal, H. S. Caram, Effect of moisture on yield locus of granular materials: theory of shift, PowderTechnology **99**, 220-227 (1998).

[6]Klausner, J. F., Chen, D., & Mei, R., Experimental investigation of cohesive powder rheology, Powder Technology, **112**(1-2), 94-101 (2000)

[7]Muzzio F.J., Goodridge C.L., Alexander A., Arratia P., Yang H., Sudah O., Mergen G., Sampling and characterization of pharmaceutical powders and granular blends, International Journal of Pharmaceutics **250**(1), pp. 51-64 (2003).

[8]Emery E., Oliver J., Pugsley T., Sharma J., Zhou J., Flowability of moist pharmaceutical powders, Powder Technology **189** (3), pp. 409-415 (2009).

[9]G. Lumay, F. Boschini, K. Traina, S. Bontempi, J.-C. Remy, R. Cloots, N. Vandewalle, Measuring the flowing properties of powders and grains, Powder Technology **224**, 19-27 (2012).

[10]Z. Liu, Q. Li, J. Zhang, Effect of moisture content on flow behavior and resistance characteristics of dense-phase pneumatic conveying, Powder Technology **387**, p. 1-8 (2021)

[11]Richefeu V., M.S. El Youssoufi, F. Radjai, Shear strength properties of wet granular materials, Phys. Rev. E **73** (5), 051304 (2006).

[12]Badetti, M., Fall, A., Chevoir, F., J.-N. Roux, Shear strength of wet granular materials: Macroscopic cohesion and effective stress, Eur. Phys. J. E **41**, 68 (2018).

[13]M. Badetti, A. Fall, D. Hautemayou, F. Chevoir, P. Aimedieu, S. Rodts, and J.-N. Roux, Rheology and microstructure of unsaturated wet granular materials: Experiments and simulations, J. of Rheology 62, 1175, doi: 10.1122/1.5026979 (2018)

[14]S. Deboeuf and A. Fall, Cohesion and aggregates in unsaturated wet granular flows down a rough incline, Journal of Rheology **67** (4), 909-909 (2023)

[15]A. Gans, O. Pouliquen, M. Nicolas, Cohesion-controlled granular material, Phys. Rev. E **101**, 032904 (2020).

[16]Mandal, S., M. Nicolas, and O. Pouliquen, Insights into the rheology of cohesive granular media, Proc. Natl. Acad. Sci. U.S.A. **117**, 8366-8373 (2020).

[17]F. Radjai, V. Richefeu, Contact dynamics as a nonsmooth discrete element method, Mech. Mater. **41**, 715-728 (2009)

[18]L. Staron, A. Abramian, Time steps vs cohesion in non-smooth contact dynamics algorithm, Proceedings of the 14th WCCM - Eccomas Congress, Vol. **300** (2021).

[19]N. Berger, E. Azéma, J.-F. Douce, F. Radjai, Scaling behaviour of cohesive granular flows Europhys. Lett. **112** 6, 64004 (2015).

[20]Khamseh, S. , J.-N. Roux, F. Chevoir, Flow of wet granular materials: a numerical study, Phys. Rev. E **92**, 022201 (2015).

[21]T. T. Vo, S. Nezamabadi, P. Mutabaruka, J.-Y. Delenne, F. Radjai, Additive rheology of complex granular flows, Nature communications **11** (1), 1-8 (2020).

[22]T. T. Vo, P. Mutabaruka, S. Nezamabadi, J.-Y. Delenne, F. Radjai, Evolution of wet agglomerates inside inertial shear flow of dry granular materials, Physical Review E **101** (3), 032906 (2020).

[23]A. Abramian, L. Staron, P.Y. Lagrée, The slumping of a cohesive granular column: Continuum and discrete modelling, J. Rheol. **64**, 1227-1235 (2020).

[24]Rognon P. G. , J.-N. Roux, M. Naaïm and F. Chevoir, Dense flows of cohesive granular materials, J. Fluid Mech. vol. **596**, pp. 21–47 (2008).

[25]Vinh Du Than, Saeed Khamseh, Anh Minh Tang, Jean-Michel Pereira, François Chevoir, and Jean-Noel Roux, Basic Mechanical Properties of Wet Granular Materials: A DEM Study. Journal of Engineering Mechanics, American Society of Civil Engineers, **143** (1), (2017)

[26]Iordanoff, Ivan, Nicolas Fillot, and Yves Berthier, Numerical study of a thin layer of cohesive particles under plane shearing, Powder Technology **159**, no. 1 (2005): 46-54.

[27]C. Mériaux, T. Triantafillou, Scaling the final deposits of dry cohesive granular columns after collapse and quasi-static fall, Physics of Fluids **20** (3), 033301 (2008).

[28]R. Artoni, A.C. Santomaso, F. Gabrieli, D. Tono, S. Cola, Collapse of quasi-two-dimensional wet granular columns, Physical Review E **87** (3), 032205 (2013)

[29]Santomaso, Andrea Claudio, Silvia Volpato, and Fabio Gabrieli, Collapse and runout of granular columns in pendular state, Physics of Fluids **30**, 6 (2018): 063301.

[30]Bougouin, A., Lacaze, L., Bonometti, T. Collapse of a liquid-saturated granular column on a horizontal plane. Phys. Rev. Fluids **4**(12), 124306 (2019).

[31]Li, P., Wang, D., Wu, Y., Niu, Z., Experimental study on the collapse of wet granular column in the pendular state, Powder Technology **393**, 357-367 (2021).

[32]A. Abramian, P.Y. Lagrée, L. Staron, How cohesion controls the roughness of a granular deposit, Soft Matter **17** (47), 10723-10729 (2021).

[33]J. Heyman, The stability of a vertical cut, Int. J. of Mech. Sci. **15**(10), 845-854 (1973)

[34]A. Gans, A. Abramian, P.-L. Lagrée, M. Gong, A. Sauret, O. Pouliquen and M. Nicolas, Collapse of a cohesive granular column, *J. Fluid Mech.* **959**, A41 (2023)

[35]Kadau D., Bartels G., Brendel L. D. E. Wolf, Contact dynamics simulations of compacting cohesive granular systems, Computer Physics Communications **147**, 190-193 (2002).

[36]L. Staron, A. Abramian and P.-Y. Lagrée, Capturing the failure of a cohesive granular step, EPJ WC **249**, 08006 (2021)

[37]Nase, S. T., W. L. Vargas, A. A. Abatan, and J. McCarthy, Discrete characterization tools for cohesive granular material, Powder Technol. **116**, 214-

223 (2001).
[38] C. M. Martin, The use of adaptive finite-element limit analysis to reveal slip-line fields, Géotechnique Letters **1**-2, 23-29 (2011)
[39] S. Mandal, M. Nicolas, O. Pouliquen, Rheology of Cohesive Granular Media: Shear Banding, Hysteresis, and Nonlocal Effects, Physical Review X 11 (2), 021017 (2021).
[40] A. Gans, Rheology of cohesive powders: experiments and modelisation, Phd thesis, Aix-Marseille University (2021).
[41] Courrech du Pont S., P. Gondret, B. Perrin, M. Rabaud Granular avalanches in fluids, Phys. Rev. Lett. **90** (4), 44301 (2003)
[42] GDR MiDi, On dense granular flows, Eur. Phys. J. E **14**, 341-365 (2004)
[43] R.M. Nedderman, *Statics and kinematics of granular materials*, Cambridge University Press (1992).
[44] F. Restagno, Bocquet L., Charlaix E., Where does a cohesive granular heap break, Eur. Phys. J. E **14**, 177-183 (2004).
[45] F. Ma, L. Duchemin, P.-Y. Lagrée, L. Staron, Failure of a cohesive granular column, in preparation